IQGAP2 regulates blood-brain barrier immune dynamics

Ketaki A. Katdare[1], Andrew Kjar[2], Natasha M. O'Brown[3], Emma H. Neal[4], Alexander G. Sorets[2], Alena Shostak[5], Wilber Romero-Fernandez[5], Alexander J. Kwiatkowski[4], Kate Mlouk[4], Hyosung Kim[4], Rebecca P. Cowell[4], Katrina R. Schwensen[4], Kensley B. Horner[4], John T. Wilson[2,4], Matthew S. Schrag[1,5,6], Sean G. Megason[3], Ethan S. Lippmann[1,2,4,5,6*]

[1]Vanderbilt Brain Institute, Vanderbilt University, Nashville, TN, USA

[2]Department of Biomedical Engineering, Vanderbilt University, Nashville, TN, USA

[3]Department of Systems Biology, Harvard Medical School, Boston, MA, USA

[4]Department of Chemical and Biomolecular Engineering, Vanderbilt University, Nashville, TN, USA

[5]Department of Neurology, Vanderbilt University Medical Center, Nashville, TN, USA

[6]Vanderbilt Memory and Alzheimer's Center, Vanderbilt University Medical Center, Nashville, TN, USA

*Correspondence to Ethan S. Lippmann (ethan.s.lippmann@vanderbilt.edu)

Abstract

Brain endothelial cells (BECs) play an important role in maintaining central nervous system (CNS) homeostasis through blood-brain barrier (BBB) functions. BECs express low baseline levels of adhesion receptors, which limits entry of leukocytes. However, the molecular mediators governing this phenotype remain mostly unclear. Here, we explored how infiltration of immune cells across the BBB is influenced by the scaffold protein IQ motif containing GTPase activating protein 2 (IQGAP2). In mice and zebrafish, we demonstrate that loss of Iqgap2 increases infiltration of peripheral leukocytes into the CNS under homeostatic and inflammatory conditions. Using single-cell RNA sequencing and immunohistology, we further show that BECs from mice lacking Iqgap2 exhibit a profound inflammatory signature, including extensive upregulation of adhesion receptors and antigen-processing machinery. Human tissue analyses also reveal that Alzheimer's disease is associated with reduced hippocampal IQGAP2. Overall, our results implicate IQGAP2 as an essential regulator of BBB immune privilege and immune cell entry into the CNS.

Introduction

Maintenance of central nervous system (CNS) homeostasis is crucial for ensuring normal functions in neurons and glial cells, which are sensitive to exogenous molecules in circulation (*1*). The brain is insulated from these factors with the help of a specialized partition known as the blood-brain barrier (BBB). The BBB is composed of barrier-forming brain endothelial cells (BECs) with unique cellular machinery that regulate the entry of macromolecules and solutes into the brain (*2*), including transporters that control the bidirectional exchange of nutrients and waste and tight junctions that prevent passive leakage of blood components into the brain (*3*).

In addition to modulating molecular transport, BECs also act as a selective interface between the peripheral immune system and the brain (*4*). Until recently, the CNS was considered to be completely isolated from the peripheral immune system and therefore an immune-privileged organ (*5*, *6*). However, recent evidence shows that the CNS is under constant immune surveillance to identify and resolve mediators of injury (*7*, *8*). For example, microglia are tissue resident innate immune cells that continually inspect the CNS parenchyma (*9*, *10*). Further, interstitial fluid and cerebrospinal fluid provide drainage pathways for prospective antigens to reach the periphery and stimulate immune cells (*11–14*). As such, initiation of an inflammatory response in the CNS can lead to recruitment of leukocytes across the BBB. BECs facilitate this process through the expression of various receptors, such as leukocyte adhesion molecules (LAMs), that allow interactions with and extravasation of leukocytes into tissue beds (*15*, *16*). In addition, BEC chemokine signaling and antigen presentation (*17–19*) also play a key role in orchestrating leukocyte extravasation. While the underlying molecular mechanisms of leukocyte extravasation are similar across all organs, BECs have been shown to express very low levels of LAMs under homeostatic conditions, making them refractory to mild inflammatory cues (*1*, *20*). However, despite several exquisite single-cell RNA sequencing (scRNA-seq) studies identifying differentially expressed genes between BECs and peripheral endothelial cells (*21–26*), as well as scRNA-seq profiles of different cell types in the

51 neurovascular unit (*24*, *25*), the mechanisms underlying suppression of LAM expression in BECs and
52 general limitation of immune cell extravasation across the BBB remain poorly understood.

53 IQ motif containing GTPase activating protein 1 (IQGAP1), a ubiquitously expressed scaffolding protein,
54 has been recently implicated in facilitating leukocyte trafficking across peripheral endothelium (*27*, *28*).
55 Historically, IQGAP1 was known as a regulator of cellular signaling due to its role as a scaffolding protein
56 (*29*). It also acts as an oncogene driving hepatocellular carcinogenesis (*30*, *31*). Interestingly, IQ motif
57 containing GTPase activating protein 2 (IQGAP2), a related member of the same scaffolding protein
58 family, acts as a tumor suppressor to counteract the oncogenic effects of IQGAP1 (*32*, *33*). Since IQGAP2
59 is believed to suppress IQGAP1 function, and IQGAP2 expression is predicted in multiple neurovascular
60 support cells such as astrocytes and microglia (*21*, *34–36*), we hypothesized that IQGAP2 may influence
61 inflammatory responses and leukocyte extravasation at the BBB. Herein, using multiple *in vivo* models, we
62 show that loss of Iqgap2 increases leukocyte infiltration into the CNS under various conditions. scRNA-
63 seq of BECs from wildtype and Iqgap2$^{-/-}$ mice further reveals an upregulation of multiple inflammatory
64 genes and signaling pathways involved in BBB-immune cell interactions. Further, using postmortem human
65 brain tissue, we determined that IQGAP2 was reduced in the hippocampus of patients with AD. Overall,
66 our results benchmark IQGAP2 as a key molecular player involved in BBB-immune crosstalk and
67 leukocyte entry into the CNS.

68

69 ## Results

70 **Global loss of Iqgap2 increases peripheral immune cell infiltration into the brain in a mouse model**
71 **of acute neuroinflammation**

72 To initially assess whether murine Iqgap2 influences leukocyte infiltration into the brain, we delivered
73 interleukin 1-beta (IL1β) into the lateral ventricles of wildtype and Iqgap2$^{-/-}$ mice (129S background) to
74 induce acute neuroinflammation (*37*, *38*). After 24 hours, infiltration of leukocytes was assessed by
75 immunohistochemical labeling of CD45+ cells in cortical brain sections. We measured a significant
76 increase in the number of CD45+ cells in the cortex of Iqgap2$^{-/-}$ mice as compared to their wildtype
77 littermates (Figure 1). We also confirmed that delivery of saline to the lateral ventricles in a similar fashion
78 did not stimulate CD45+ cell infiltration into the brains of both wildtype and Iqgap2$^{-/-}$ mice (Figure 1B).
79 These data suggest that Iqgap2 constrains leukocyte infiltration into the mouse CNS following a central
80 inflammatory challenge.

81

82 **Global loss of Iqgap2 increases immune cell infiltration in experimental autoimmune**
83 **encephalomyelitis**

84 As dysregulated immune cell infiltration is a hallmark of several neurodegenerative conditions (*39–45*), we
85 sought to next evaluate whether loss of Iqgap2 affects immune cell access to the CNS in the presence of an
86 inflammatory neurodegenerative condition. As such, to monitor the effects of Iqgap2 loss under a chronic
87 inflammatory insult (*46*), we induced experimental autoimmune encephalomyelitis (EAE) in wildtype and
88 Iqgap2$^{-/-}$ 129S mice (Figure 2A). To validate our experimental strategy, we concurrently induced EAE in
89 C57BL/6 mice and observed robust development of disease (Supplementary Figure 1). We measured a
90 significant increase in CD45+ cells in the Iqgap2$^{-/-}$ lumbar spinal cord compared to wildtype 129S mice 30
91 days after EAE induction (Figure 2B). Interestingly, this increase in infiltrating leukocytes did not produce
92 significant differences in disease severity, probability of survival, or demyelination (Figure 2C-E),

93 suggesting the infiltration events may be decoupled from pathology. Overall, these data further indicate that
94 loss of Iqgap2 contributes to increased leukocyte extravasation into the CNS under extended
95 neuroinflammation.

96

97 **Loss of Iqgap2 increases infiltration of peripheral immune cells into the brain in zebrafish in the**
98 **absence of inflammation**

99 Our data in multiple inflammatory mouse models suggest that Iqgap2 plays an important role in BBB
100 immune privilege. To corroborate these findings in an additional species, we generated zebrafish crispants
101 by direct injection of Cas9 protein with multiple sgRNAs to target genes of interest in single-cell embryos
102 with both endothelial cells (kdrl:mCherry) and immune cells (mpeg1:EGFP) transgenically labeled. We
103 specifically assessed the presence of mpeg+ macrophage lineage cells in the brains of 5 days post
104 fertilization (dpf) zebrafish, which have a functional BBB (*47*), that were either uninjected or targeting *tyr*
105 or *iqgap2.* While uninjected fish are expected to retain normal function of all genes, *tyr* crispants should
106 have mosaic knockout of tyrosinase*,* a protein involved in pigment production that is not expected to affect
107 leukocyte infiltration; this serves as an additional CRISPR injection control*.* Both controls displayed
108 similarly low numbers of mpeg+ cells in the brain, while *iqgap2* crispants displayed a significant increase
109 in the number of mpeg+ cells (Figure 3B). Since mpeg also labels brain resident microglia, we used an
110 established method to label microglia with Neutral Red dye (*48*) and distinguish these cells from infiltrating
111 leukocytes. Uninjected controls and *iqgap2* crispants were therefore treated with Neutral Red and all
112 mpeg+/Neutral Red+ double-positive microglia and mpeg+/Neutral Red- infiltrating leukocytes were
113 quantified throughout the entire zebrafish brain. We measured a significant increase in the total number of
114 mpeg+ cells, similar to previous experiments, but not double-positive microglia in the *iqgap2* crispants,
115 and the number of mpeg+/Neutral Red- infiltrating leukocytes was significantly increased (Figure 3C).
116 These data suggest that *iqgap2* is essential for restricting the infiltration of leukocytes into the CNS under

homeostatic conditions in zebrafish, as its mosaic depletion enhanced the entry of peripheral leukocytes into the brain.

Global loss of Iqgap2 yields a profound inflammatory transcriptomic profile in mouse BECs

Our data indicate that Iqgap2 plays an important role in restricting peripheral immune access to the CNS and in modulating responses to inflammatory insults. Iqgap2 is a large scaffolding protein known to orchestrate many different cellular functions such as regulating cytoskeletal organization, cytokinesis, and carcinogenesis (*29*), suggesting it could govern many different signaling axes that would influence BBB function and cellular crosstalk within the neurovascular unit. After confirming general expression of Iqgap2 in mouse brain and enriched vessel fractions (Supplementary Figure 2), we performed scRNA-seq on BECs isolated from wildtype and Iqgap2$^{-/-}$ mice to better understand how loss of Iqgap2 affects BBB function. Here, to generate an endothelial cell-enriched population for sequencing, we isolated antibody-labeled CD31+ cells from dissociated mouse brains using fluorescence-activated cell sorting (Figure 4A). After implementing quality control metrics, cells were first analyzed using dimension-reduction by uniform manifold approximation and projection (UMAP) and unsupervised clustering to obtain 12 unique identities: endothelial cells (EC), PLVAP-expressing endothelial cells (EC_plvap), hemoglobin-expressing endothelial cells (EC_hb), endothelial/stromal cells or pericyte-like cells (EC/PC), endothelial/stromal cells or astrocyte-like cells (EC/AC), astrocytes (AC), B cells, T cells, monocytes (MNC), microglia (MG), oligodendrocytes (OLG), and fibroblasts (Supplementary Figure 3). Endothelial cells were the largest represented cell type, followed by immune cells such as monocytes and T cells that are also predicted to express CD31 (Figure 4B and Supplementary Figure 3); other cell types likely represent some small contamination in the sorting process. Each cell type was annotated using previously established marker genes (*49*) and all non-endothelial clusters were filtered out of the dataset for these initial analyses. Wildtype (WT) and Iqgap2$^{-/-}$ (KO) genotypes were equally represented in the EC cluster (Figure 4C), and bulk gene expression comparisons between WT and KO BECs show 928 differentially regulated genes

142 (DEGs) (Figure 4D). Since leukocyte extravasation occurs predominantly at post-capillary venules (*50–*
143 *52*), we examined these DEGs along the neurovascular tree. We used unsupervised clustering to subcluster
144 BECs into 6 sub-populations, and based on marker gene expression, these subclusters were further
145 classified into arterial (A; genes *Hey1, Bmx, and Sema3g*), capillary (C; genes *Slc16a2, Car4, and Mfsd2a*),
146 and venous (V; genes *Icam1, Slc38a5, and Vwf*) zonal identities (Figure 4E and Supplementary Figure 3)
147 (*21*). Further analysis suggests that the strongest DEGs are shared among zonal identities and include genes
148 involved in antigen presentation, interleukin receptor subunits, and adhesion molecules. Unique DEGs
149 identified in the A and V zonal identities did not show any significant functional enrichment whereas a
150 similar analysis of unique DEGs identified in the C zonal identity suggest subtle changes in BEC function
151 (Figure 4F and Supplementary Table 1).

152 Across these zones, we were able to confirm that loss of Iqgap2 does not significantly affect expression of
153 most canonical BBB genes, including junction proteins and nutrient transporters such as *Cdh5, Cldn5, Ocln,*
154 *Tjp,* and *Slc2a1* (Supplementary Figure 4A). At the protein level, total vessel density was unchanged, and
155 we found no obvious deficits in expression of claudin-5, occludin, ZO-1, and Glut1 in the Iqgap2$^{-/-}$ mice
156 (Supplementary Figure 5). We did observe significant differences in gene expression for certain transporters
157 that facilitate exchange of amino acids and metabolites across the BBB, such as *Abcb1a*, *Slc7a1*, *Slc7a5*,
158 and *Slc16a1* (Supplementary Figure 4B). In addition, major regulator genes involved in BBB functional
159 development and maintenance like *Mfsd2a* (*53*) and *Ctnnb1* (*54–56*) were significantly downregulated in
160 the Iqgap2$^{-/-}$ BECs, suggesting possible connections to BBB dysfunction (Supplementary Figure 4C).
161 Interestingly, we also saw significant upregulation of several LAMs and chemokine receptors. Although
162 interaction with leukocytes and response to inflammation is primarily facilitated by venous ECs, we found
163 that loss of Iqgap2 significantly upregulates expression of leukocyte receptors and signaling molecules like
164 *Vcam1, Icam1,* and *Ackr1* across multiple vascular zones (Figure 5A). Using immunohistochemistry, we
165 confirmed upregulation of Vcam1 in cortical vasculature of Iqgap2$^{-/-}$ mice (Figure 5B). The widespread
166 expression of vascular Vcam1 in Iqgap2$^{-/-}$ mice was particularly striking, given that Vcam1 expression on

167 BECs has been implicated in brain inflammation and cognitive decline in mice (*57*). We have also recently
168 shown that vascular VCAM-1 expression is significantly increased in Alzheimer's disease cortex relative
169 to asymptomatic age-matched controls, further highlighting its links to human neurodegeneration (*58*).

170 To extend our understanding of potential pathways in BECs affected by global loss of Iqgap2, we performed
171 gene set enrichment analysis (GSEA) for KEGG signaling pathways. GSEA indicated that pathways
172 involved in response to infections like Kaposi sarcoma-associated herpes virus infection (KSHV), human
173 T-cell leukemia virus 1 infection (HTLV), human immunodeficiency virus 1 infection (HIV), and human
174 papillomavirus infection (HPV) were upregulated. In addition, other pathways facilitating immune
175 interactions like cell adhesion (*Vcam1, Icam1*), antigen processing and presentation (*Psme2, Hspa5, Canx,*
176 *Calr*), and TNF signaling (*Cxcl1, Csf1, Ptgs2*) were also significantly upregulated in the Iqgap2$^{-/-}$ BECs
177 (Figure 5C and Supplementary Figure 6). These results indicate that *Iqgap2* loss shifts both the
178 transcriptional profile and protein expression of BECs towards an activated, inflammatory state.

179 Due to the significant upregulation of LAMs in the Iqgap2$^{-/-}$ BECs, we further analyzed cell-cell interactions
180 between BECs and other cell types identified in the scRNA-seq dataset using CellChat (*59*). We found that
181 BEC-immune cell interactions were overrepresented in Iqgap2$^{-/-}$ mice. Quantification of these results
182 suggested an increase in cell-cell interactions between BECs and microglia as well as BECs and peripheral
183 immune cells like monocytes, T cells, and B cells. We then assessed the predicted directionality of these
184 interactions by analyzing known receptor-ligand pairs. BECs were predicted to be the "senders" whereas
185 immune populations, especially monocytes, were the primary "receivers" (Supplementary Figure 7). To
186 understand whether these changes were due to Iqgap2 loss in a specific cell type, we performed DEG
187 analyses in all clusters annotated as immune populations. Monocytes had the highest number of significant
188 DEGs, followed by microglia and T cells (Supplementary Figure 8A). KEGG pathway analysis of DEGs
189 in the monocytes indicated upregulation of pathways such as leukocyte transendothelial migration and
190 regulation of actin cytoskeleton (Supplementary Figure 8B). These data indicate that Iqgap2 may also play

191 an important role in modulating BEC-monocyte communication, which could additionally contribute to the
192 overall inflammatory phenotype observed in the BECs in Iqgap2$^{-/-}$ mice.

193

194 **IQGAP2 in postmortem human brain tissue**

195 To putatively assess connections between IQGAP2 and human disease states, we evaluated IQGAP2
196 protein distribution patterns in postmortem human hippocampal tissue from patients with Alzheimer's
197 disease (AD) and in cases without AD. Using a custom polyclonal antibody raised against a peptide with
198 selective homology to human IQGAP2, we immunostained and quantified vascular-associated and
199 parenchymal IQGAP2 signal in human hippocampal sections. IQGAP2 staining was strongly detected
200 along blood vessels (identified by collagen expression), with more diffuse and punctate signal observed in
201 the parenchyma (Figure 6). A significant decrease in IQGAP2 levels was found in parenchymal tissue (non-
202 vascular regions) in AD patients (Figure 6). Connections between immune cell entry into the brain and
203 neurodegeneration are becoming increasingly scrutinized (*60*, *61*), highlighting the potential importance of
204 this finding.

205

206 **Discussion**

207 Peripheral endothelial cells display high levels of LAMs and can respond swiftly to local and systemic
208 inflammatory cues (*62*). This is followed by rapid infiltration of leukocytes into surrounding tissue beds. In
209 comparison, BECs are comparably immune quiescent under homeostatic conditions and generally express
210 low levels of LAMs. This allows the BBB to more selectively control the activation of downstream
211 inflammatory pathways and extravasation of leukocytes into the CNS (*63*, *64*). Although peripheral immune
212 responses are essential for the resolution of CNS injury, it is well established that age-related neurological
213 deficits and chronic neurodegeneration may be exacerbated in part by unwarranted entry of leukocytes into
214 the brain (*39*, *41*, *65–67*). Further, BECs upregulate transcriptional signatures of inflammatory responses
215 during aging and neurological disease (*24*, *25*, *68*). As such, identifying mechanisms that regulate BEC
216 inflammatory responses is critical for understanding the pathological progression of these diseases and
217 developing strategies to decrease leukocyte extravasation. Our study provides evidence that IQGAP2 plays
218 an important role in BBB immune dynamics and the propensity of leukocytes to enter the CNS after immune
219 stimulation.

220 To our knowledge, the role of IQGAP proteins in BBB integrity has not been studied. *IQGAP2* belongs to
221 the *IQGAP* family of scaffolding proteins involved in orchestrating a wide array of intracellular signaling
222 and cytoskeleton dynamics (*29*). The multidomain structure of these proteins acts as a framework for
223 complex formation of signaling proteins, thus influencing many downstream cellular processes. *IQGAPs*
224 were historically considered to be modulators of cytoskeletal architecture. However, it has become apparent
225 that their role extends into other physiological processes like glomerular filtration in the kidney,
226 cardiomyocyte function in the heart, smooth muscle cell contraction in lung airways, and metabolism in the
227 liver (*29*, *69*, *70*). *IQGAP2* has also been studied in the context of its tumor-suppressive characteristics
228 (*71*). Previous studies identified *IQGAP2* as a novel tumor suppressor gene specifically linked to the
229 development of hepatocellular carcinoma. More recently, *IQGAP2* inactivation has been linked to other
230 malignancies like gastric cancer (*72*), prostate cancer (*73*), and bladder cancer (*74*). Moreover, reduced

231 expression of *IQGAP2* is associated with worsened cancer pathology and poor clinical outcomes (*73*, *75*,
232 *76*). Our study provides new context for the role of IQGAP2 in physiological processes related to immune
233 cell trafficking.

234 One limitation of our study is that we cannot exclusively ascribe the observed CNS leukocyte infiltration
235 to loss of Iqgap2 expression in a particular cell type. *IQGAP2* has generally high expression in many
236 immune cell subtypes (*77*), but this has not previously been associated with specific phenotypes like tissue
237 extravasation and responsiveness to inflammatory cytokines. Our current data may suggest that cell-to-cell
238 communication between BECs and immune cells plays a role in BBB inflammation when Iqgap2 is lost.
239 However, more extensive scRNA-seq profiling of the neurovascular unit in Iqgap2$^{-/-}$ mice, as well as
240 lineage-specific Iqgap2 knockout models, will be necessary in future studies to fully clarify cell-intrinsic
241 and cell-extrinsic effects of IQGAP2 on BBB immune privilege.

242 An additional unanswered question is whether changes in IQGAP2 expression contribute to human
243 neurodegenerative disease progression through modulation of immune cell recruitment to the CNS. In the
244 acute and chronic inflammatory animal models used in this study, we did not observe significant differences
245 in pathology. In the EAE model, it is possible that the 30-day timepoint does not reflect increased damage
246 caused by infiltrating leukocytes due to other compensatory mechanisms (e.g. significant damage could
247 occur at an earlier time point followed by regeneration), especially when considering the biphasic disease
248 severity in the Iqgap2$^{-/-}$ mice and that deaths generally occurred during periods where disease severity
249 worsened. In human hippocampal tissue, we observed a decrease in IQGAP2 in patients with AD. Single-
250 cell datasets indicate parenchymal IQGAP2 expression is restricted to microglia, while vascular IQGAP2
251 expression could potentially be localized to perivascular macrophages or fibroblasts (*21*, *24*, *36*).
252 Interestingly, microglia have been recently connected to T cell infiltration in mouse models of tauopathy
253 (*78*) and general aging (*79*), and T cell infiltration and resultant activation of microglia has been shown to
254 exacerbate neurodegeneration in engineered human cell-based models of AD (*80*). In the context of our

255 study, these findings motivate future exploration into whether loss of Iqgap2 influences pathology and
256 immune cell infiltration in mouse and human models of AD.

257 Overall, our work reveals a novel role for IQGAP2 in regulating BBB immune dynamics. While the cell-
258 specific effects of IQGAP2 are currently unclear, our collective data suggest that this protein plays an
259 important conserved and previously unrecognized role in suppressing BEC inflammatory responses and
260 regulating immune cell trafficking to the CNS through non-cell autonomous mechanisms. Future work will
261 determine these mechanisms of action and their relevance to brain disorders.

262 **Methods**

263

264 Mouse maintenance and procedures

265 Colony maintenance: All mouse protocols were approved by the Institutional Animal Care and Use
266 Committee at Vanderbilt University. Iqgap2$^{-/-}$ mice (129S background) were obtained from Jackson
267 Laboratory (strain 025452). Male and female Iqgap2$^{-/-}$ mice and wildtype littermate controls were used for
268 all experiments. Mice were at least 8 weeks of age at the time of use and were housed continuously in an
269 environmentally controlled facility in a 12-hour light/dark cycle with *ad libitum* access to food and water.

270 Genotyping: Mice were ear-tagged and tail snips were collected at approximately 2 weeks of age. Genomic
271 DNA was extracted using an Extracta DNA Prep kit for tissue (Quantabio) per manufacturer instructions.
272 DNA was extracted in the Extraction buffer at 95°C for 30 minutes, cooled to room temperature and mixed
273 with Stabilization buffer before being stored at -20°C. The reactions were performed using the Apex Hot
274 Start Taq BLUE Master Mix (Apex Bioresearch) on a ProFlex PCR system (Applied Biosystems). A
275 touchdown cycling protocol was used with an initial annealing temperature of 65°C gradually lowered to
276 60°C over the course of 10 cycles. Genotyping primers used were as follows: Mutant Reverse–
277 ATTTGTCACGTCCTGCACGACG, Wildtype Reverse–TGGCCTTCCTCCCTTAAAGT, and Common
278 Forward–TGACTCAGAGGGCACATGGT. PCR products were run on a 2% agarose-TAE buffered gel
279 supplemented with SYBR Safe DNA Gel Stain (Invitrogen) and imaged using a LI-COR Odyssey Fc gel
280 imager (Supplementary Figure 9).

281 Tissue collection: Mice were deeply anesthetized using high-dose isoflurane and euthanized by transcardial
282 perfusion of 1X DPBS (Gibco), followed by 4% paraformaldehyde (PFA, Thermo Fisher Scientific). Brains
283 and lumbar segment of spinal cords were extracted and postfixed in 4% PFA overnight followed by
284 cryopreservation in sucrose gradient solutions (15% and 30%, respectively). The tissue was then embedded

285 in OCT medium (Tissue-Tek) and 15 µm (brain) and 25 µm (spinal cord) thick sections were cut and stored
286 at -80ºC.

287 Microvessel isolation: Mice were deeply anesthetized using high-dose isoflurane and euthanized by
288 decapitation. Brains were extracted and collected in ice-cold PBS. Microvessels from the cortex were
289 isolated as previously described (*81*). In brief, cortices were dissected from remaining brain tissue,
290 homogenized in PBS using a tissue homogenizer (Wheaton), and collected by centrifugation. Homogenized
291 tissue was resuspended in a 15% dextran solution (~70,000 kDa, Sigma) and centrifuged at 10,000xg to
292 separate the vessel fraction from the remaining tissue. The vessel fraction was washed with PBS and filtered
293 using a 40 µm cell strainer (Corning). For protein extraction, the vessel fraction was incubated in RIPA
294 buffer (Sigma) supplemented with 1% v/v protease and phosphatase inhibitor cocktails (Sigma) for 30-60
295 minutes on ice. Cell debris was separated by centrifugation (12,000xg for 15 minutes at 4ºC) and the
296 supernatant was stored at -20ºC. Protein concentration was quantified using a Pierce BCA Protein Assay
297 (Thermo Fisher Scientific) according to the manufacturer instructions. For immunohistochemical analysis,
298 microvessel suspension was placed on glass slides and allowed to dry at room temperature. Dried
299 microvessels were then fixed with 4% parafolmaldehyde solution and labelled with Lectin DyLight 488 for
300 30 minutes at room temperature before mounting in Prolong Gold Antifade Mountant (Invitrogen).

301 Intracerebroventricular injection of IL1β: Male and female Iqgap2$^{-/-}$ mice and wildtype littermates were
302 used as experimental animals. All animals were at least 12 weeks old at the time of the surgery. Under
303 isoflurane anesthesia, mice were unilaterally injected into the lateral ventricle using a stereotactic apparatus
304 at coordinates of AP = -0.3 mm, ML = -1 mm, and DV = -3 mm. After injections, mice were returned to
305 prewarmed home cages for recovery. Each mouse received 20 ng/µL of IL1β solution (20 ng in 1 µL PBS)
306 or an equivalent volume of sterile PBS. 24 hours after surgery, mice were transcardially perfused with PBS
307 followed by 4% paraformaldehyde and brains were extracted for immunohistological analysis. For
308 quantification, CD45+ cells were manually counted in each section under blinded conditions. Vasculature

309 was labelled using a fluorescence-conjugated GLUT1 antibody to solely quantify CD45+ cells that had
310 extravasated out of the vessels into the brain parenchyma.

311 Experimental autoimmune encephalomyelitis (EAE): Female Iqgap2$^{-/-}$ mice and wildtype littermates were
312 used as experimental animals. All animals were between 9 and 13 weeks of age at the time of induction.
313 EAE kits (Hooke Laboratories) targeting MOG_{35-55} antigen were used. 100 µL of MOG_{35-55}/Complete
314 Freund's Adjuvant emulsion was injected subcutaneously at the scruff of the neck and near the base of the
315 tail resulting in a total injection volume of 200 µL into each mouse. At 2 and 24 hours post injection of
316 emulsion, 100 µL of pertussis toxin (4 µg/mL) was injected intraperitoneally. Clinical scores were evaluated
317 starting 7 days post induction as follows: score 1, flaccid tail; score 2, weak hind limbs; score 3, hind limb
318 paralysis; score 4, quadriplegia. Clinical scores were recorded every day for the first week after
319 development of symptoms followed by every other day thereafter. Premature deaths were recorded. 30 days
320 following induction, mice were transcardially perfused with PBS followed by 4% paraformaldehyde. Brains
321 and spinal cords were extracted for immunohistological analysis. For quantification, CD45+ cells were
322 manually counted in each section under blinded conditions. Vasculature was labelled using a fluorescence-
323 conjugated GLUT1 antibody to ensure that CD45+ cells had extravasated out of the vessels. For quantifying
324 EAE pathology in spinal cord, total area and demyelination area were calculated using the "Measure" tool
325 in ImageJ by manually outlining regions of interest as indicated by Luxol Fast Blue stain.

326

327 Zebrafish maintenance and procedures

328 Zebrafish were maintained at 28.5°C following standard protocols (*82*). All zebrafish work was approved
329 by the Harvard Medical Area Standing Committee on Animals under protocol number IS00001263-3. Adult
330 fish were maintained on a standard light-dark cycle from 8 am to 10 pm. Adult fish, aged 3 months to 1.5
331 years, were crossed to produce embryos and larvae. For imaging live larvae, 0.003% phenylthiourea (PTU)
332 was used beginning at 1 dpf to inhibit melanin production. These studies used the AB wildtype strains and

333 the transgenic reporter strains (Tg(kdrl:HRAS-mCherry)^{s896} (*83*), abbreviated as Tg(kdrl:mCherry), and
334 Tg(mpeg1:EGFP)^{gl22} (*84*), abbreviated as Tg(mpeg1:EGFP). Mosaic *iqgap2* crispants were generated by
335 injection of 7 µM Cas9 protein complexed with four sgRNAs (5'-AGTAGCCTCGATTTACAGG-3', 5'-
336 GCACTTTGTCAGTCACGGAA-3', 5'-CAGGACAGCGCGAGCACTG-3', and 5'-AAAGTCCGCGCG
337 CAGTTTA-3') to target multiple sites in the *iqgap2* transcript, and *tyr* control crispants were similarly
338 targeted with four sgRNAs (5'-GCCGCACACAGAGCCGTCGC-3', 5'-GGATGCATTATTACGTGTCC
339 -3', 5'- GACTCTACATCGGCGGATGT-3', and 5'-GTATCCGTCGTTGTGTCCGA-3'). To distinguish
340 between microglia and macrophages, 4 dpf larvae were exposed to 2.5 µg/ml of Neutral Red (Millipore
341 Sigma: N7005) in embryo water for 3 hours at 28.5°C. Larvae were washed at least three times to remove
342 the residual dye and then microglia were assessed the next day as previously described (*48*). Zebrafish
343 larvae were immobilized by tricaine exposure and live imaged on a Leica SP8 line scanning confocal
344 microscope. Quantification of mpeg+ and Neutral Red+ cells was manually performed on blinded z-stack
345 images that spanned the entire larval head using ImageJ.

346

347 <u>Human brain tissue and preparation</u>

348 Human brain tissue was obtained at autopsy and prepared as previously described (*85*). De-identified brain
349 tissue was obtained from the Vanderbilt Brain and Biospecimen Bank at Vanderbilt University Medical
350 Center. Written informed consent for brain donation was obtained from patients or their surrogate decision
351 makers. All brain tissue collection was authorized by the Institutional Review Board at Vanderbilt
352 University Medical Center. Demographics and neuropathological information for each donor are listed in
353 Supplementary Table 2.

354 Human brain tissue was obtained at autopsy and immersion fixed in 10% formalin (Thermo Fisher
355 Scientific) at 4ºC for 1-3 days. The fixative solution was then removed and the tissued rinsed with 1x TBS
356 (Corning) three times for 5 minutes each. The tissue was placed in sterile 10% sucrose (Millipore Sigma)

357 /1x TBS/0.02% sodium azide (NaN_3, Millipore Sigma) until tissue sank and then 30% sucrose/1x
358 TBS/0.02% NaN_3 for overnight at 4ºC or until the tissue sank. The tissue block was affixed to the stage of
359 vibratome using cyanoacrylate cement and fully submerged in 1x TBS. Hippocampal sections were
360 prepared at 50 µm thickness. Floating tissue sections were transferred to 15 mL Falcon tubes with antigen
361 retrieval buffer (10 mM citric acid pH 6.0, Millipore Sigma) containing 0.05% Tween-20 (Millipore Sigma)
362 and heated to 95˚C for 20 minutes in a block heater. Hippocampal sections were then washed with 100 mM
363 glycine (Millipore Sigma)/1x TBS/0.1% Triton X-100 (Millipore Sigma) buffer for 30 minutes followed
364 by permeabilization with 0.3% Triton X-100/1x TBS buffer for 30 minutes and two washes for 5 minutes
365 each with 1x TBS at room temperature.

366

367 Development of a custom antibody against human IQGAP2 protein

368 A peptide corresponding to amino acid residues 1460-1474 of human IQGAP2 (RSIKLDGKGEPKGAK)
369 was synthesized with an amino-terminal cysteine and conjugated to maleimide-activated Keyhole Limpet
370 Haemocyanin (KLH), maleimide-activated bovine serum albumin (BSA), and SulfoLink resin using
371 manufacturer protocols (Thermo Fisher). The peptide-KLH conjugate was used to immunize rabbits
372 (Cocalico Biologicals). Rabbit antisera were tested for the presence of antibodies recognizing the IQGAP2
373 peptide by dot blot analysis using the peptide-BSA conjugate. The rabbit antibodies were affinity-purified
374 from the antisera using the peptide-SulfoLink resin, where 5 mL of rabbit sera was diluted 1:1 with PBS
375 and passed over a 2 mL peptide-SulfoLink column. After extensive washing with PBS, bound antibodies
376 were eluted with 8.5 mL 0.1 M Glycine (pH 2.2) and collected in a tube containing 1.5 mL of 1 M Tris (pH
377 8). Antibody solution was stored at -80°C.

378

379 Immunofluorescent staining

380 Mouse tissue: Tissue slices were retrieved from the -80ºC freezer and allowed to thaw at room temperature
381 for 10-15 minutes. Sections were washed with 1X PBS with 0.03% Triton X-100 to remove the OCT
382 medium. Sections were then blocked using a goat serum blocking buffer and incubated in primary antibody
383 solution overnight at 4°C. After incubation, primary antibody solution was thoroughly washed off and
384 sections were incubated in secondary antibody solution for 2 hours at room temperature. All antibodies and
385 corresponding dilutions used for immunohistochemistry are listed in Supplementary Tables 3-4. Following
386 final washes, tissue was mounted in Prolong Gold Antifade Mountant with DAPI (Invitrogen) and slides
387 were allowed to dry overnight before imaging on a Leica DMi8 epifluorescence microscope. All acquired
388 images were processed and quantified using ImageJ software. For quantification of vascular Vcam1
389 expression, mean Vcam1 intensity was calculated within CD31+ vessels using ImageJ.

390 Human tissue: Immunohistochemical labeling in hippocampal tissue slices was performed as previously
391 described (*85*, *86*) with minor modifications. Tissue slices were incubated with primary antibodies for 48
392 hours at 4ºC followed by secondary antibodies for 2 hours at room temperature. All antibodies and
393 corresponding dilutions used for immunohistochemistry are listed in Supplementary Tables 3-4. Neuritic
394 plaques, neurofibrillary tangles and related AD pathological structures were additionally stained using 1
395 μM 4,4'-[(2-methoxy-1,4-phenylene) di-(1*E*)-2,1-ethenediyl] bisphenol (MX-04) (Tocris) for 15 minutes
396 at room temperature. Confocal images were acquired using the Zeiss LSM 710 confocal laser-scanning
397 microscope (Carl Zeiss AG) with a 20× air/dry or 63× oil objective and 10 μm z-stack scanning projections
398 with a step interval of 1 μm or one scanning projection, with a minimum resolution of 1500 x 1500 pixels.
399 Vascular IQGAP2 expression was quantified using mean IQGAP2 intensity within Collagen+ area and
400 parenchymal IQGAP2 expression was quantified by gating Collagen- area using ImageJ.

401

402 Luxol Fast Blue staining

403 Tissue slices were retrieved from the -80ºC freezer and allowed to thaw at room temperature for 10-15
404 minutes. Sections were first allowed to dry overnight at room temperature and then immersed in a 70%
405 ethanol solution overnight to facilitate defatting. Luxol Fast Blue stain (Abcam) was applied to the sections
406 and incubated for 5 to 6 hours at 60ºC. Excess stain was washed off by consecutive dipping in fresh absolute
407 ethanol. Slides were differentiated briefly using lithium carbonate solution and washed with distilled water
408 and alcohol solution. Lastly, sections were counterstained with Cresyl Etch Violet, washed with distilled
409 water, dehydrated with absolute alcohol and mounted in DPX mounting medium (Sigma-Aldrich).
410 Mounting medium was cured overnight before imaging on a Leica DMi8 inverted microscope.

411

412 Western blotting

413 Protein samples from mouse tissue were prepared by diluting 20-40 µg of protein with 1X Laemmli buffer
414 (Biorad) supplemented with beta-mercaptoethanol (Sigma) and Ultrapure water (Gibco) to a final volume
415 of 20-30 µL. Samples were then boiled at 95ºC for 5 minutes, cooled on ice, and centrifuged briefly.
416 Samples were then loaded into 4-20% Criterion TGX Midi protein gels (Biorad) along with Precision Plus
417 Dual Color Protein ladder (Biorad) and run at 80-120V. Protein gels were then transferred onto iBlot2
418 Nitrocellulose membranes (Thermo Fisher Scientific) using an iBlot2 transfer device (Thermo Fisher
419 Scientific). Membranes were cut to size and blocked for at least 30 minutes at room temperature in Intercept
420 TBS Blocking buffer (LI-COR Biosciences) on a shaker. Membranes were submerged in primary
421 antibodies diluted in blocking buffer with 0.05% Tween20 (Sigma) and incubated at 4ºC overnight.
422 Following primary antibody incubation, membranes were washed in wash buffer (1X tris buffered saline
423 with 0.05% Tween-20). Membranes were incubated in secondary antibodies diluted in the wash buffer at
424 room temperature for 2 hours. All primary and secondary antibody information is listed in Supplementary
425 Tables 3-4. Blots were imaged using a LI-COR Odyssey Clx or Fc Imager and bands were quantified using
426 Image Studio Lite software.

427

428 Single-cell RNA sequencing

429 Fresh cortical tissue was homogenized and delipidated using an Adult Brain Dissociation Kit (Miltenyi
430 Biotec) according to the manufacturer's instructions. The resultant single-cell suspension was incubated
431 with TruStain FcX (Biolegend) for 10 minutes at 4°C to prevent non-specific antibody binding of Fc
432 receptors, labeled with a secondary conjugated CD31 antibody (1:2000, eBioscience) for 30 minutes, and
433 counterstained with DAPI. Live CD31+ cells were flow sorted using a 4-laser FACS Aria III sorter (BD
434 Biosciences) at the Vanderbilt Flow Cytometry Shared Resource. Live cells were resuspended in DMEM
435 (Gibco) supplemented with 2% FBS to obtain a concentration of 700-1200 cells/μL. RNA extraction, 10X
436 Genomics Chromium 5' scRNAseq Library Prep, and sequencing on an Illumina NovaSeq6000 sequencer
437 was performed at the VANTAGE core facility.

438

439 Single-cell RNA sequencing analysis

440 All gene by counts data were read into Seurat (v.4). The initial data were filtered to retain only cells with
441 RNA counts between 1,200 and 20,000 (with less than 10% being mitochondrial). Within each biological
442 experiment, data were log normalized. The top 2,000 variable features (as identified by variance) were
443 selected. Samples were combined using CCA (Seurat v.4) and then standardized. UMAP based on the first
444 50 principal components was used to reduce dimensionality for visualization and clustering (*87*). Predicted
445 doublets were filtered out using DoubletFinder (*88*). Unsupervised clustering was achieved using the KNN-
446 graph approach in Seurat (*89*), and clusters were annotated with SingleR (*90*) based on previously published
447 datasets (*49*). Predominantly endothelial clusters (0,2,4,5) were rescaled and clustered based on the first 15
448 principal components. Clusters were annotated as arterial, capillary, or venous based on the expression of
449 established marker gene sets (*21*). Approximately 2,000 ECs were analyzed per condition. Differentially
450 expressed genes (DEGs) were computed in Seurat using the FindMarkers() function with built-in

Bonferroni correction. KEGG or Reactome gene set enrichment analysis (GSEA) was computed on significant DEGs using WebGestalt with a false discovery rate cutoff of 0.05 and weighted set cover redundancy reduction (*91*). Communication between cell types was predicted using the CellChat R packages (*59*). For visualization, *EnhancedVolcano* (*92*), *UpSetR* shiny app (*93*), *iGraph* (*94*), and *ggvenn* were employed.

Statistical analysis

Statistical analysis for single-cell RNA sequencing data was conducted in R. All other analysis was performed in GraphPad Prism 9.0.0.

Data availability

Raw sequencing data files have been deposited in the ArrayExpress collection under accession code E-MTAB-12687. All code used for the single-cell RNA sequencing analyses is publicly available at: https://github.com/LippmannLab/IQGAP2_WT_KO_BEC_scRNAseq.

Author contributions

KAK, ESL, and EHN conceived the study. KAK and ESL designed the majority of experiments with input from the other authors. KAK, NMO, EHN, AGS, AS, AJK, HK, and RPC conducted all experiments. AK performed all bioinformatics analyses. KM assisted with data quantification. WRF performed human tissue histology. KRS and KBH provided support on animal husbandry and takedowns for experiments. MSS provided human tissue samples and contributed to interpretation of histological images. JTW and SGM provided input on experimental planning and data interpretation.

Acknowledgments

Funding was provided by a Chan Zuckerberg Initiative Ben Barres Early Career Acceleration Award (grant 2019-191850 to ESL) and NIH grant R21 NS106510 (to ESL). AK and EHN were supported by the National Science Foundation Graduate Research Fellowship Program. NMO was supported by a Damon Runyon Postdoctoral Fellowship. Support for RNA sequencing was provided by Vanderbilt Technologies for Advanced Genomics core facility, which is supported by the CTSA Grant (NIH grant 5UL1 RR024975), the Vanderbilt Ingram Cancer Center (NIH grant P30 CA68485), the Vanderbilt Vision Center (NIH grant P30 EY08126), and NIH/NCRR grant G20 RR030956. Support for histology was provided by Vanderbilt Translational Pathology Shared Resource core facility, which is supported by P30 CA068485. Flow cytometry experiments were performed in the Vanderbilt Flow Cytometry Shared Resource, which is supported by P30 CA068485 and the Vanderbilt Digestive Disease Research Center (P30 DK058404). The custom IQGAP2 antibody in this study was produced by the Vanderbilt Antibody and Protein Resource, which was supported by P30 CA068485. Image acquisition was performed in part through the use of the Vanderbilt Cell Imaging Shared Resource, which is supported by NIH grants P30 CA68485, P30 DK20593, P30 EY08126, and S10RR027396. The authors thank Dr. Jose Gomez for early assistance with the Iqgap2$^{-/-}$ mice and Dr. Eric Shusta for sharing microarray data that initially indicated the potential relevance of IQGAP2. Some figures in this manuscript were created in part using BioRender.

Competing interests

The authors declare no competing interests.

495 **Figures**

496

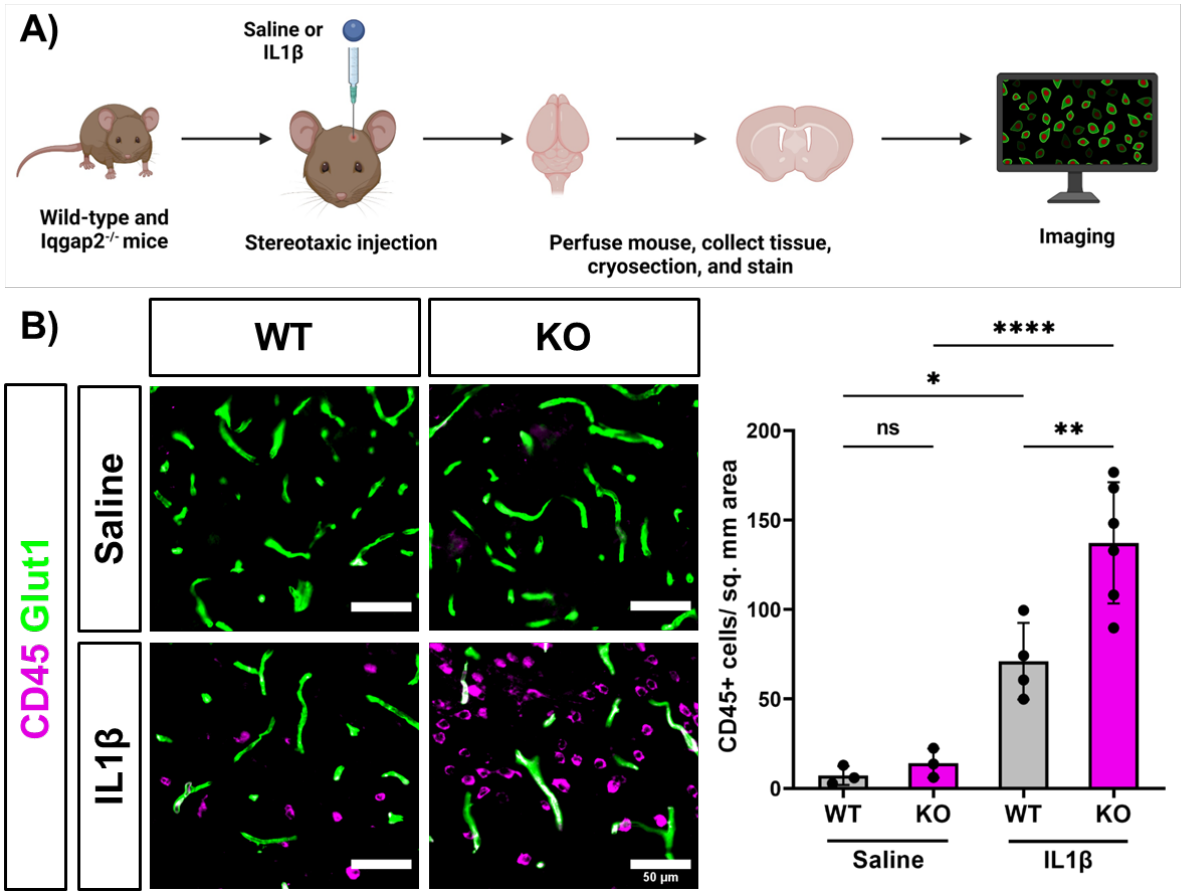

497

498 **Figure 1: Global loss of Iqgap2 increases infiltration of peripheral leukocytes in a mouse model of**

499 **acute neuroinflammation.**

500 A) Schematic representation of experimental design for assessing leukocyte numbers in mouse brains 24

501 hours after intracerebroventricular saline or IL1β delivery.

502 B) Representative images and quantification of CD45+ immune cells (magenta) and vasculature (green)

503 in wildtype (WT) and Iqgap2$^{-/-}$ (KO) mouse brain cortex following treatment with saline or IL1β. Data

504 are represented as mean ± SD, and each data point represents an individual mouse, where at least 5

505 images were quantified per mouse. For saline treatment, N=3 WT mice and N=3 KO mice, and for

506 IL1β treatment, N=4 WT mice and N=6 KO mice. Statistical significance was calculated using one-
507 way ANOVA with Tukey's multiple comparison's test (*, $p<0.05$, **, $p<0.01$, ****$p<0.0001$).
508

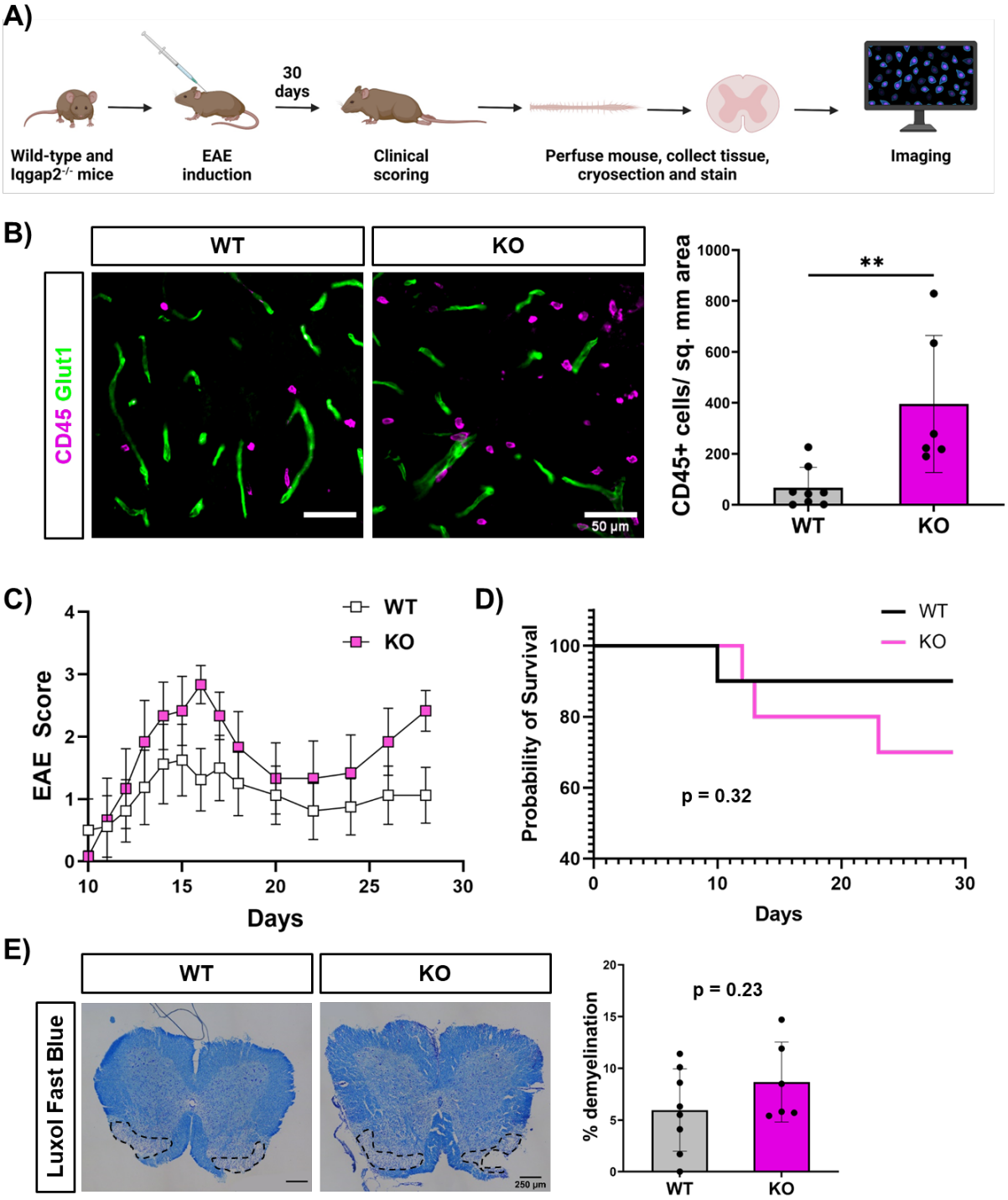

Figure 2: Global loss of Iqgap2 increases infiltration of peripheral leukocytes in EAE.

A) Schematic representation of experimental design for assessing response to EAE 30 days following induction.

513 B) Representative images and quantification of CD45+ immune cells (magenta) and vasculature (green)
514 in wildtype (WT) and Iqgap2$^{-/-}$ (KO) lumbar spinal cord at 30 days following EAE induction. Data are
515 represented as mean ± SD, and each data point represents an individual mouse. At least 8 images were
516 quantified per mouse. N=8 WT mice, N=6 KO mice. Statistical significance was calculated using the
517 unpaired student's t-test (**, $p<0.01$).
518 C) EAE score curve for wildtype (WT) and Iqgap2$^{-/-}$ (KO) mice following EAE induction. Data are
519 presented as mean ± SEM. N=8 WT mice, N=6 KO mice. Statistical significance was calculated using
520 the unpaired student's t-test on area under the curve.
521 D) Probability of survival in WT versus KO mice following EAE induction. N=10 WT and KO mice.
522 Statistical significance was calculated using Log-rank (Mantel-Cox) test.
523 E) Representative images and quantification of demyelinating lesions in WT and KO lumbar spinal cord
524 section stained with Luxol Fast Blue at 30 days following EAE induction. Data are represented as mean
525 ± SD, and each data point represents an individual mouse, where 1 image was quantified per mouse.
526 N=8 WT mice, N=6 KO mice. Statistical significance was calculated using the unpaired student's t-
527 test.

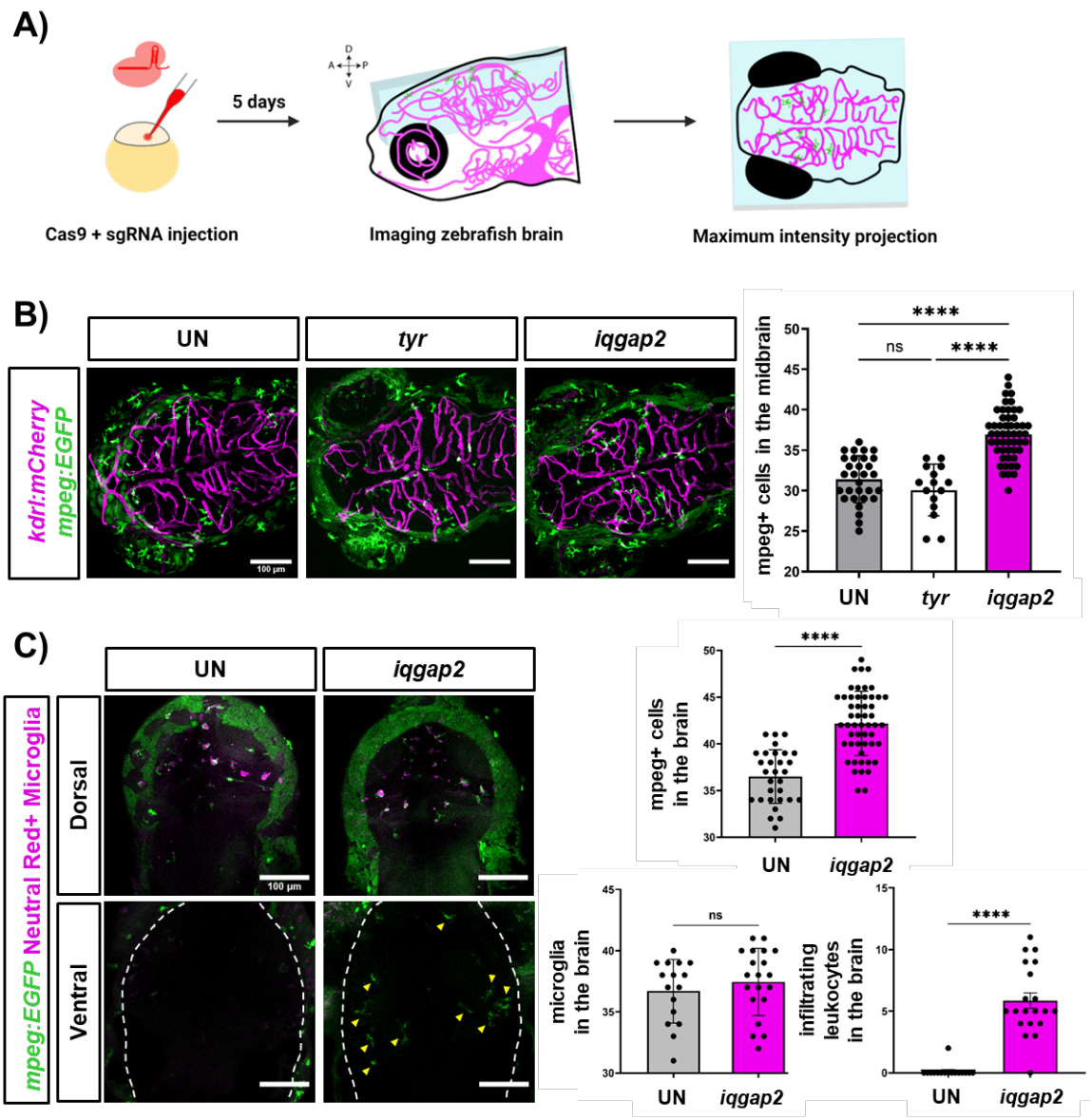

Figure 3: Mosaic loss of *iqgap2* expression increases infiltration of peripheral immune cells into the zebrafish brain.

A) Schematic representation of experimental design for assessing leukocyte numbers in the larval zebrafish brain. Double transgenic (kdrl:mCherry; mpeg:EGFP) single-cell embryos were injected with Cas9 protein and sgRNAs to target genes of interest. These mosaic crispants were then allowed to develop normally, and mpeg+ leukocytes were quantified in the brain at 5 dpf.

535 B) Representative 100 µm thick maximum intensity projection images and quantification of macrophage
536 lineage cells (mpeg:EGFP) in the brains of uninjected (UN) controls, *tyr* crispant controls, and *iqgap2*
537 crispants. Vasculature is marked with the kdrl:mCherry transgene (magenta). N=30 fish (UN), 15 fish
538 (*tyr*), and 52 fish (*iqgap2*). Data are represented as mean ± SD, and each data point represents an
539 individual fish. Statistical significance was calculated using a one-way ANOVA with Tukey's multiple
540 comparison's test (****, $p<0.0001$).

541 C) Representative images and quantification of infiltrating leukocytes versus tissue-resident microglia in
542 the brains of *iqgap2* crispants versus uninjected (UN) controls. Representative 30 µm thick maximum
543 intensity projection images of the dorsal (top) or ventral (bottom) brain regions and quantification of
544 mpeg+ (green) macrophage lineage cells and mpeg+/Neutral Red+ (magenta) microglia. Yellow
545 arrowheads indicate individual mpeg+/Neutral Red- infiltrating leukocytes in the ventral brain of
546 *iqgap2* crispants. N=16 fish (UN) and 20 fish (*iqgap2*). Data represented as mean ± SD, and each data
547 point represents an individual fish. Statistical significance was calculated using an unpaired Student's
548 t-test (****, $p<0.0001$).

549

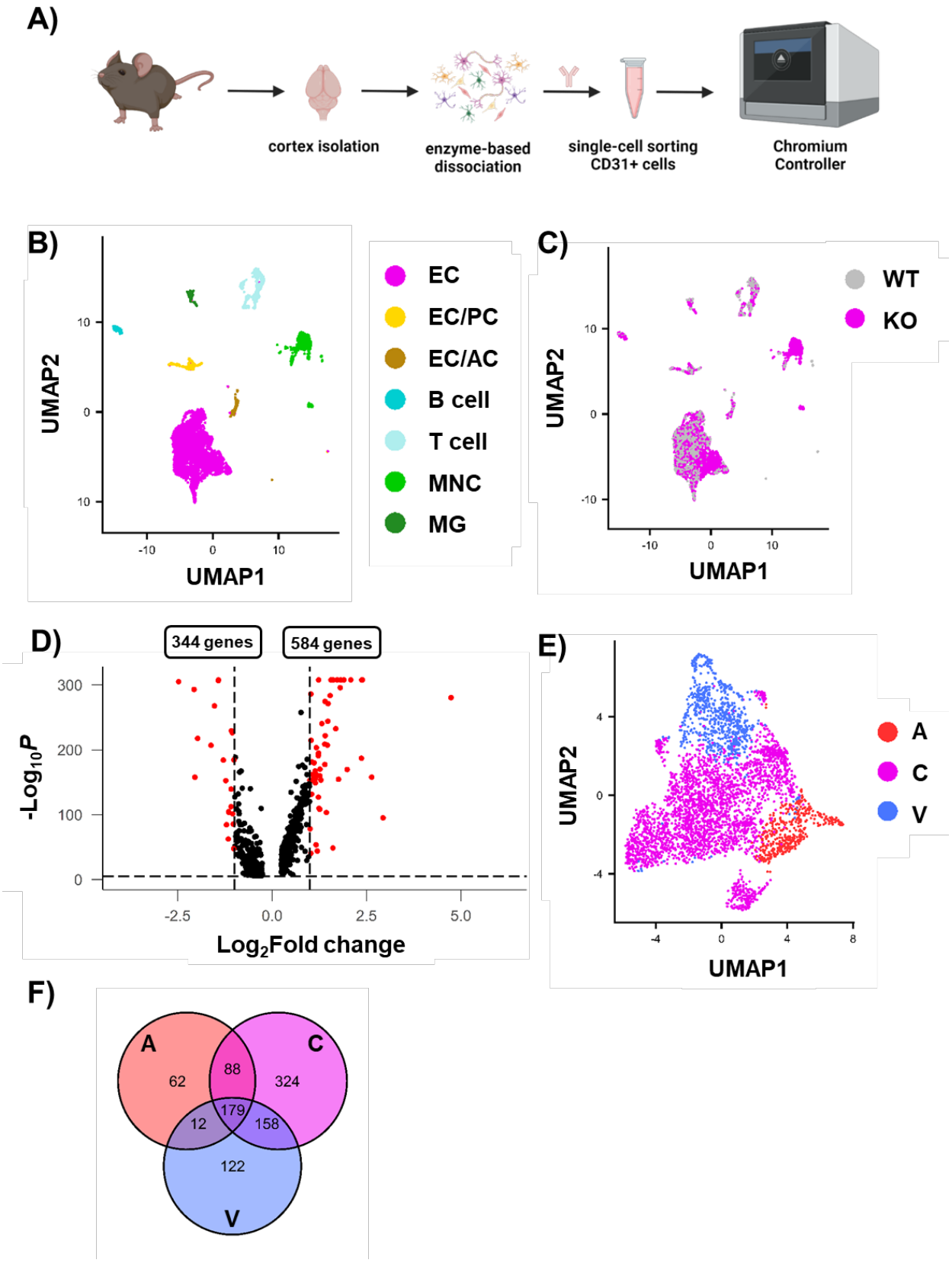
A)
cortex isolation
enzyme-based dissociation
single-cell sorting CD31+ cells
Chromium Controller
B)
UMAP2
UMAP1
EC
EC/PC
EC/AC
B cell
T cell
MNC
MG
C)
WT
KO
UMAP2
UMAP1
D)
344 genes
584 genes
-Log10P
Log2Fold change
E)
A
C
V
UMAP2
UMAP1
F)
A
C
V
62
88
324
179
12
158
122

550

551 **Figure 4: Global loss of Iqgap2 yields extensive transcriptional changes in BECs.**

552 A) Schematic representation of experimental design. Whole brain cortices were isolated from wildtype
553 (WT) and Iqgap2$^{-/-}$ (KO) mice, dissociated to a single cell suspension using enzyme-based dissociation
554 techniques, and sorted to enrich for CD31+ cells before sequencing.

555 B) UMAP cell annotations based on unsupervised clustering. EC = endothelial cells, EC/PC = EC/stromal
556 cells (pericytes), EC/AC = EC/stromal cells (astrocytes), MNC = monocytes, MG = microglia.

557 C) UMAP comparison between WT (grey) and KO (pink) cells.

558 D) Volcano plot highlighting differentially expressed genes in the EC cluster. 928 genes were significantly
559 altered, with 584 upregulated and 344 downregulated by loss of Iqgap2. Red dots indicate genes with
560 $p<0.05$ and >2-fold change in expression.

561 E) UMAP of endothelial zonal identity based on unsupervised clustering. A = arterial, C = capillary, V =
562 venous.

563 F) Venn diagram showing number of DEGs shared between zonal identities.

564

565

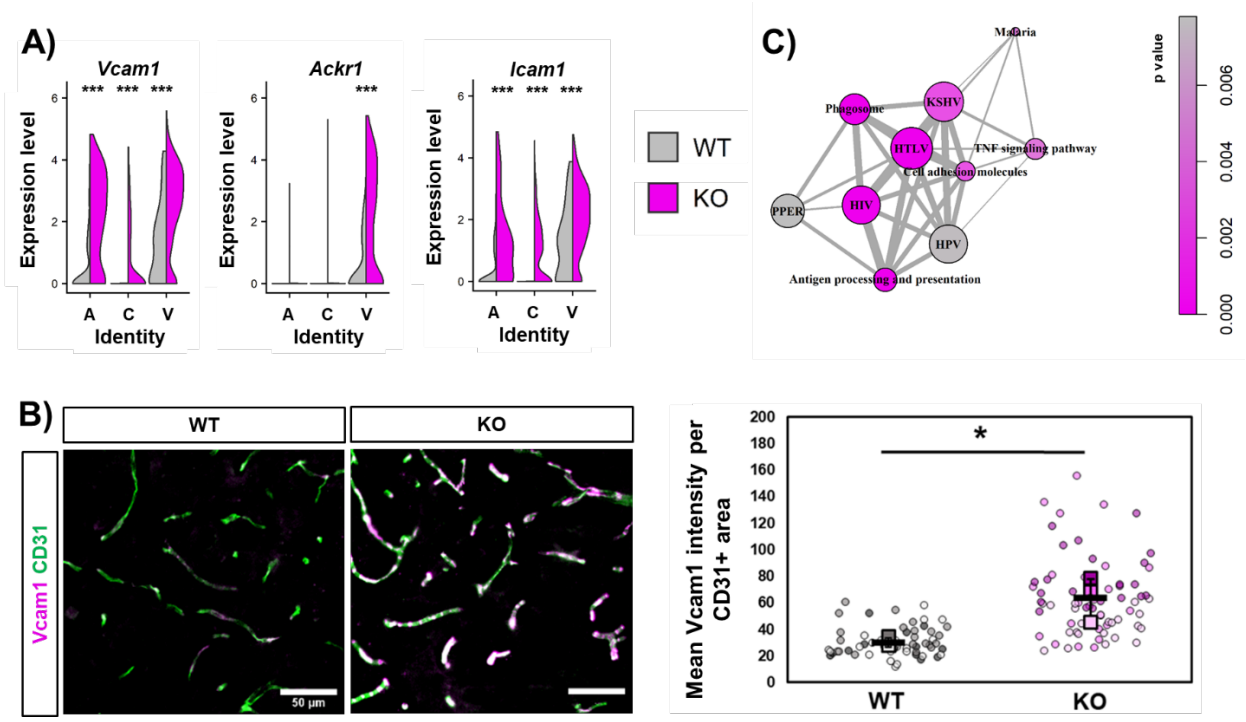

Figure 5: Global loss of Iqgap2 produces a widespread inflammatory phenotype in BECs.

A) Split violin plots indicating differential gene expression of select inflammatory markers across vascular zones between wildtype (WT) and Iqgap2$^{-/-}$ (KO) BECs. Statistical significance was calculated using Wilcox rank-order tests with Bonferroni correction (***, $p<0.001$).

B) Representative images and quantification of vascular Vcam1 expression in WT versus KO mouse cortex. Quantification was performed across N=3 biological replicates. Data are represented as mean ± SD (black bars). Biological replicates are represented as squares and measurements from individual images are represented as circles color coded to each replicate. Statistical significance was calculated using the student's unpaired t-test (*, $p<0.05$).

C) GSEA analysis for signaling pathways upregulated in KO versus WT BECs. Each node represents an enriched gene set belonging to the labeled canonical pathway. Nodes are colored based on p-value, and thickness of the connecting lines indicates similarity of overlapping genes represented in connected gene sets. KSHV = Kaposi sarcoma-associated herpes virus infection, HTLV = Human T-cell leukemia

580 virus 1 infection, HIV = Human immunodeficiency virus 1 infection, PPER = Protein processing in

581 endoplasmic reticulum, HPV = Human papillomavirus infection.

582

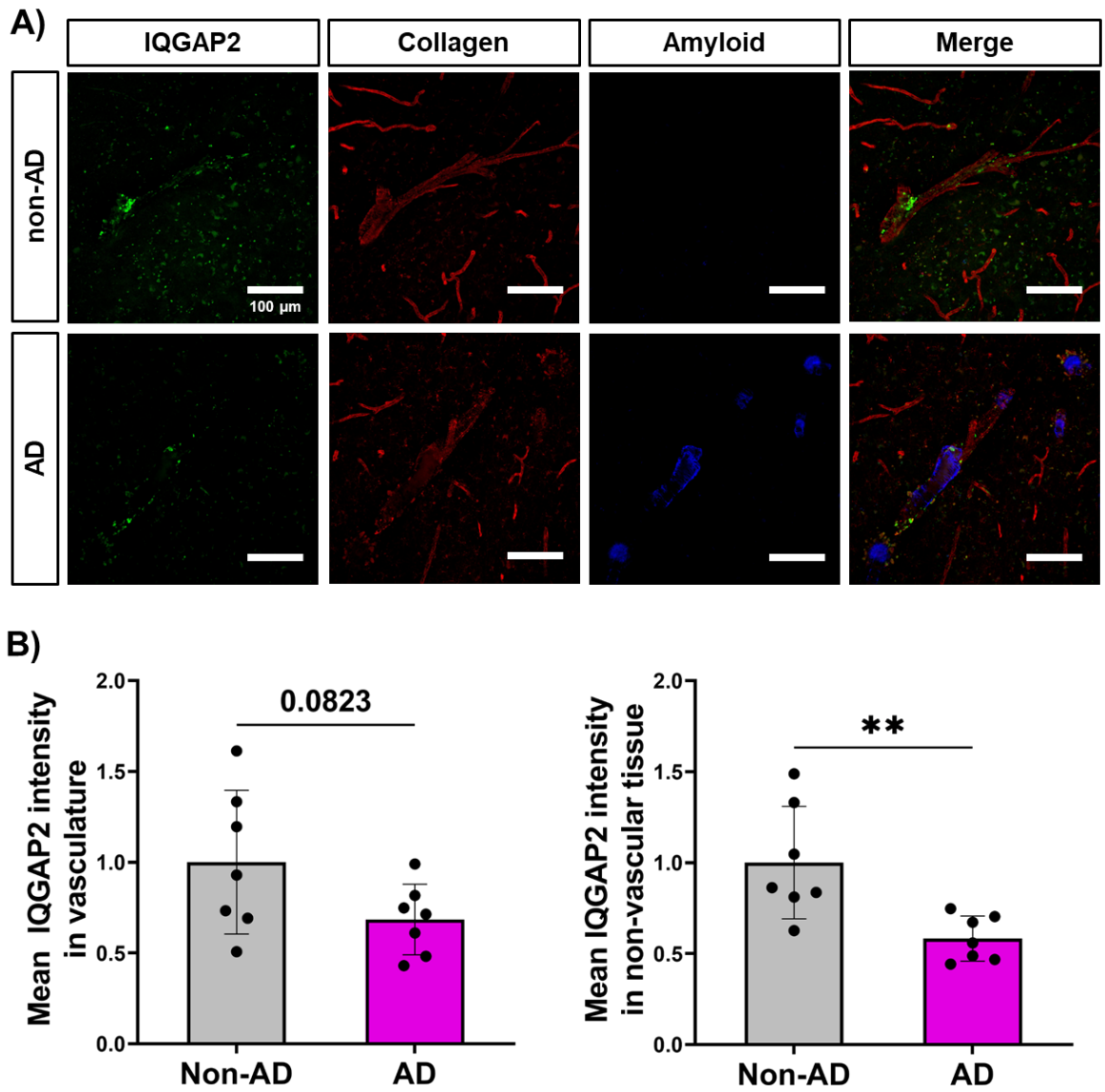

Figure 6: IQGAP2 distribution in human hippocampus.

A) Representative confocal microscopy images of IQGAP2 (green) in human hippocampal tissue from AD and non-AD donors. Images were produced from 10 µm z-stack scanning projections with a step interval of 1 µm. Vasculature was stained with Collagen (red) and β-amyloid and neuritic plaques, neurofibrillary tangles and other tau aggregates were stained with Methoxy-X04 (blue).

B) Mean IQGAP2 intensity in vascular regions was quantified solely one scanning projection in collagen+ area, while IQGAP2 intensity in parenchyma was quantified by gating samples to

591 exclude collagen+ area. Data are presented as mean ± SD, where each data point represents an
592 individual donor with at least five images quantified per donor. N=7 non-AD donors and N=7 AD
593 donors. Statistical significance was calculated using unpaired student's t-test (**, $p<0.01$).

594

595 **References**

596 1. C. P. Profaci, R. N. Munji, R. S. Pulido, R. Daneman, The blood–brain barrier in health and disease:
597 Important unanswered questions. *J. Exp. Med.* **217**, e20190062 (2020).

598 2. R. Daneman, A. Prat, The Blood–Brain Barrier. *Cold Spring Harb. Perspect. Biol.* **7**, a020412 (2015).

599 3. B. Obermeier, R. Daneman, R. M. Ransohoff, Development, maintenance and disruption of the blood-
600 brain barrier. *Nat. Med.* **19**, 1584–1596 (2013).

601 4. B. Engelhardt, C. Coisne, Fluids and barriers of the CNS establish immune privilege by confining
602 immune surveillance to a two-walled castle moat surrounding the CNS castle. *Fluids Barriers CNS*
603 **8**, 4 (2011).

604 5. A. Louveau, T. H. Harris, J. Kipnis, Revisiting the Mechanisms of CNS Immune Privilege. *Trends*
605 *Immunol.* **36**, 569–577 (2015).

606 6. B. Engelhardt, P. Vajkoczy, R. O. Weller, The movers and shapers in immune privilege of the CNS.
607 *Nat. Immunol.* **18**, 123–131 (2017).

608 7. L. Marchetti, B. Engelhardt, Immune cell trafficking across the blood-brain barrier in the absence and
609 presence of neuroinflammation. *Vasc. Biol.* **2**, H1–H18 (2020).

610 8. J. A. Mapunda, H. Tibar, W. Regragui, B. Engelhardt, How Does the Immune System Enter the Brain?
611 *Front. Immunol.* **13**, 805657 (2022).

612 9. G. Raivich, Like cops on the beat: the active role of resting microglia. *Trends Neurosci.* **28**, 571–573
613 (2005).

614 10. S. S. Ousman, P. Kubes, Immune surveillance in the central nervous system. *Nat. Neurosci.* **15**, 1096–
615 1101 (2012).

616 11. J. D. Laman, R. O. Weller, Drainage of Cells and Soluble Antigen from the CNS to Regional Lymph
617 Nodes. *J. Neuroimmune Pharmacol.* **8**, 840–856 (2013).

618 12. A. Louveau, B. A. Plog, S. Antila, K. Alitalo, M. Nedergaard, J. Kipnis, Understanding the functions
619 and relationships of the glymphatic system and meningeal lymphatics. *J. Clin. Invest.* **127**, 3210–
620 3219 (2017).

621 13. B. Engelhardt, R. O. Carare, I. Bechmann, A. Flügel, J. D. Laman, R. O. Weller, Vascular, glial, and
622 lymphatic immune gateways of the central nervous system. *Acta Neuropathol. (Berl.)* **132**, 317–338
623 (2016).

624 14. S. P. das Neves, N. Delivanoglou, S. Da Mesquita, CNS-Draining Meningeal Lymphatic Vasculature:
625 Roles, Conundrums and Future Challenges. *Front. Pharmacol.* **12**, 655052 (2021).

626 15. B. Engelhardt, R. M. Ransohoff, The ins and outs of T-lymphocyte trafficking to the CNS: anatomical
627 sites and molecular mechanisms. *Trends Immunol.* **26**, 485–495 (2005).

628 16. B. Engelhardt, R. M. Ransohoff, Capture, crawl, cross: the T cell code to breach the blood–brain
629 barriers. *Trends Immunol.* **33**, 579–589 (2012).

630 17. S. Aydin, J. Pareja, V. M. Schallenberg, A. Klopstein, T. Gruber, N. Page, E. Bouillet, N. Blanchard,
631 R. Liblau, J. Körbelin, M. Schwaninger, A. J. Johnson, M. Schenk, U. Deutsch, D. Merkler, B.
632 Engelhardt, Antigen recognition detains CD8+ T cells at the blood-brain barrier and contributes to its
633 breakdown. *Nat. Commun.* **14**, 3106 (2023).

634 18. C. E. Fain, J. Zheng, F. Jin, K. Ayasoufi, Y. Wu, M. T. Lilley, A. R. Dropik, D. M. Wolf, R. C.
635 Rodriguez, A. Abudumijiti, Z. P. Tritz, S. M. Bouchal, L. L. Pewe, S. L. Urban, Y. Chen, S.-Y. Chang,
636 M. J. Hansen, J. M. Kachergus, J. Shi, E. A. Thompson, H. E. Jensen, J. T. Harty, I. F. Parney, J. Sun,
637 L.-J. Wu, A. J. Johnson, Discrete class I molecules on brain endothelium differentially regulate
638 neuropathology in experimental cerebral malaria. *Brain*, awad319 (2023).

639 19. M. A. Lopes Pinheiro, A. Kamermans, J. J. Garcia-Vallejo, B. van het Hof, L. Wierts, T. O'Toole, D.
640 Boeve, M. Verstege, S. M. van der Pol, Y. van Kooyk, H. E. de Vries, W. W. Unger, Internalization
641 and presentation of myelin antigens by the brain endothelium guides antigen-specific T cell migration.
642 *eLife* **5**, e13149 (2016).

643 20. I. Galea, The blood–brain barrier in systemic infection and inflammation. *Cell. Mol. Immunol.* **18**,
644 2489–2501 (2021).

645 21. M. Vanlandewijck, L. He, M. A. Mäe, J. Andrae, K. Ando, F. Del Gaudio, K. Nahar, T. Lebouvier,
646 B. Laviña, L. Gouveia, Y. Sun, E. Raschperger, M. Räsänen, Y. Zarb, N. Mochizuki, A. Keller, U.
647 Lendahl, C. Betsholtz, A molecular atlas of cell types and zonation in the brain vasculature. *Nature*
648 **554**, 475–480 (2018).

649 22. M. F. Sabbagh, J. S. Heng, C. Luo, R. G. Castanon, J. R. Nery, A. Rattner, L. A. Goff, J. R. Ecker, J.
650 Nathans, Transcriptional and epigenomic landscapes of CNS and non-CNS vascular endothelial cells.
651 *eLife* **7**, e36187 (2018).

652 23. J. Kalucka, L. P. M. H. de Rooij, J. Goveia, K. Rohlenova, S. J. Dumas, E. Meta, N. V. Conchinha,
653 F. Taverna, L.-A. Teuwen, K. Veys, M. García-Caballero, S. Khan, V. Geldhof, L. Sokol, R. Chen,
654 L. Treps, M. Borri, P. de Zeeuw, C. Dubois, T. K. Karakach, K. D. Falkenberg, M. Parys, X. Yin, S.
655 Vinckier, Y. Du, R. A. Fenton, L. Schoonjans, M. Dewerchin, G. Eelen, B. Thienpont, L. Lin, L.
656 Bolund, X. Li, Y. Luo, P. Carmeliet, Single-Cell Transcriptome Atlas of Murine Endothelial Cells.
657 *Cell* **180**, 764-779.e20 (2020).

658 24. A. C. Yang, R. T. Vest, F. Kern, D. P. Lee, M. Agam, C. A. Maat, P. M. Losada, M. B. Chen, N.
659 Schaum, N. Khoury, A. Toland, K. Calcuttawala, H. Shin, R. Pálovics, A. Shin, E. Y. Wang, J. Luo,
660 D. Gate, W. J. Schulz-Schaeffer, P. Chu, J. A. Siegenthaler, M. W. McNerney, A. Keller, T. Wyss-
661 Coray, A human brain vascular atlas reveals diverse mediators of Alzheimer's risk. *Nature* **603**, 885–
662 892 (2022).

663 25. F. J. Garcia, N. Sun, H. Lee, B. Godlewski, H. Mathys, K. Galani, B. Zhou, X. Jiang, A. P. Ng, J.
664 Mantero, L.-H. Tsai, D. A. Bennett, M. Sahin, M. Kellis, M. Heiman, Single-cell dissection of the
665 human brain vasculature. *Nature* **603**, 893–899 (2022).

666 26. E. A. Winkler, C. N. Kim, J. M. Ross, J. H. Garcia, E. Gil, I. Oh, L. Q. Chen, D. Wu, J. S. Catapano,
667 K. Raygor, K. Narsinh, H. Kim, S. Weinsheimer, D. L. Cooke, B. P. Walcott, M. T. Lawton, N. Gupta,
668 B. V. Zlokovic, E. F. Chang, A. A. Abla, D. A. Lim, T. J. Nowakowski, A single-cell atlas of the
669 normal and malformed human brain vasculature. *Science* **375**, eabi7377 (2022).

670 27. D. P. Sullivan, P. J. Dalal, F. Jaulin, D. B. Sacks, G. Kreitzer, W. A. Muller, Endothelial IQGAP1
671 regulates leukocyte transmigration by directing the LBRC to the site of diapedesis. *J. Exp. Med.* **216**,
672 2582–2601 (2019).

673 28. D. P. Sullivan, P. J. Dalal, D. B. Sacks, W. A. Muller, Calcium Signaling Regulates Leukocyte
674 Transendothelial Migration through the Action of Endothelial Cell IQGAP1, Calmodulin, and
675 CaMKIIδ. *FASEB J.* **34**, 1–1 (2020).

676 29. J. M. Smith, A. C. Hedman, D. B. Sacks, IQGAPs choreograph cellular signaling from the membrane
677 to the nucleus. *Trends Cell Biol.* **25**, 171–184 (2015).

678 30. Q. Dai, Q. Ain, M. Rooney, F. Song, A. Zipprich, Role of IQ Motif-Containing GTPase-Activating
679 Proteins in Hepatocellular Carcinoma. *Front. Oncol.* **12**, 920652 (2022).

680 31. X. Jin, Y. Liu, J. Liu, W. Lu, Z. Liang, D. Zhang, G. Liu, H. Zhu, N. Xu, S. Liang, The Overexpression
681 of IQGAP1 and β-Catenin Is Associated with Tumor Progression in Hepatocellular Carcinoma In
682 Vitro and In Vivo. *PLOS ONE* **10**, e0133770 (2015).

683 32. C. D. White, H. Khurana, D. V. Gnatenko, Z. Li, R. D. Odze, D. B. Sacks, V. A. Schmidt, IQGAP1
684 and IQGAP2 are Reciprocally Altered in Hepatocellular Carcinoma. *BMC Gastroenterol.* **10**, 125
685 (2010).

686 33. V. A. Schmidt, C. S. Chiariello, E. Capilla, F. Miller, W. F. Bahou, Development of Hepatocellular
687 Carcinoma in *Iqgap2* -Deficient Mice Is IQGAP1 Dependent. *Mol. Cell. Biol.* **28**, 1489–1502 (2008).

688 34. Y. Zhang, K. Chen, S. A. Sloan, M. L. Bennett, A. R. Scholze, S. O'Keeffe, H. P. Phatnani, P.
689 Guarnieri, C. Caneda, N. Ruderisch, S. Deng, S. A. Liddelow, C. Zhang, R. Daneman, T. Maniatis,
690 B. A. Barres, J. Q. Wu, An RNA-Sequencing Transcriptome and Splicing Database of Glia, Neurons,
691 and Vascular Cells of the Cerebral Cortex. *J. Neurosci.* **34**, 11929–11947 (2014).

692 35. Y. Zhang, S. A. Sloan, L. E. Clarke, C. Caneda, C. A. Plaza, P. D. Blumenthal, H. Vogel, G. K.
693 Steinberg, M. S. B. Edwards, G. Li, J. A. Duncan, S. H. Cheshier, L. M. Shuer, E. F. Chang, G. A.
694 Grant, M. G. H. Gephart, B. A. Barres, Purification and Characterization of Progenitor and Mature
695 Human Astrocytes Reveals Transcriptional and Functional Differences with Mouse. *Neuron* **89**, 37–
696 53 (2016).

697 36. L. He, M. Vanlandewijck, M. A. Mäe, J. Andrae, K. Ando, F. Del Gaudio, K. Nahar, T. Lebouvier,
698 B. Laviña, L. Gouveia, Y. Sun, E. Raschperger, Å. Segerstolpe, J. Liu, S. Gustafsson, M. Räsänen,
699 Y. Zarb, N. Mochizuki, A. Keller, U. Lendahl, C. Betsholtz, Single-cell RNA sequencing of mouse
700 brain and lung vascular and vessel-associated cell types. *Sci. Data* **5**, 180160 (2018).

701 37. M. G. Proescholdt, S. Chakravarty, J. A. Foster, S. B. Foti, E. M. Briley, M. Herkenham,
702 Intracerebroventricular but not intravenous interleukin-1β induces widespread vascular-mediated
703 leukocyte infiltration and immune signal mRNA expression followed by brain-wide glial activation.
704 *Neuroscience* **112**, 731–749 (2002).

705 38. X. Liu, D. P. Nemeth, D. B. McKim, L. Zhu, D. J. DiSabato, O. Berdysz, G. Gorantla, B. Oliver, K.
706 G. Witcher, Y. Wang, C. E. Negray, R. S. Vegesna, J. F. Sheridan, J. P. Godbout, M. J. Robson, R.
707 D. Blakely, P. G. Popovich, S. D. Bilbo, N. Quan, Cell-Type-Specific Interleukin 1 Receptor 1
708 Signaling in the Brain Regulates Distinct Neuroimmune Activities. *Immunity* **50**, 764–766 (2019).

709 39. S. Amor, F. Puentes, D. Baker, P. van der Valk, Inflammation in neurodegenerative diseases.
710 *Immunology* **129**, 154–169 (2010).

711 40. D. Gate, E. Tapp, O. Leventhal, M. Shahid, T. J. Nonninger, A. C. Yang, K. Strempfl, M. S. Unger,
712 T. Fehlmann, H. Oh, D. Channappa, V. W. Henderson, A. Keller, L. Aigner, D. R. Galasko, M. M.
713 Davis, K. L. Poston, T. Wyss-Coray, CD4 $^{+}$ T cells contribute to neurodegeneration in Lewy body
714 dementia. *Science* **374**, 868–874 (2021).

715 41. D. Gate, N. Saligrama, O. Leventhal, A. C. Yang, M. S. Unger, J. Middeldorp, K. Chen, B. Lehallier,
716 D. Channappa, M. B. De Los Santos, A. McBride, J. Pluvinage, F. Elahi, G. K.-Y. Tam, Y. Kim, M.
717 Greicius, A. D. Wagner, L. Aigner, D. R. Galasko, M. M. Davis, T. Wyss-Coray, Clonally expanded
718 CD8 T cells patrol the cerebrospinal fluid in Alzheimer's disease. *Nature* **577**, 399–404 (2020).

719 42. M. S. Unger, E. Li, L. Scharnagl, R. Poupardin, B. Altendorfer, H. Mrowetz, B. Hutter-Paier, T. M.
720 Weiger, M. T. Heneka, J. Attems, L. Aigner, CD8+ T-cells infiltrate Alzheimer's disease brains and
721 regulate neuronal- and synapse-related gene expression in APP-PS1 transgenic mice. *Brain. Behav.*
722 *Immun.* **89**, 67–86 (2020).

723 43. R. H. Earls, J.-K. Lee, The role of natural killer cells in Parkinson's disease. *Exp. Mol. Med.* **52**, 1517–
724 1525 (2020).

725 44. B. Hemmer, M. Kerschensteiner, T. Korn, Role of the innate and adaptive immune responses in the
726 course of multiple sclerosis. *Lancet Neurol.* **14**, 406–419 (2015).

727 45. J. Stephenson, E. Nutma, P. Van Der Valk, S. Amor, Inflammation in CNS neurodegenerative
728 diseases. *Immunology* **154**, 204–219 (2018).

729 46. C. S. Constantinescu, N. Farooqi, K. O'Brien, B. Gran, Experimental autoimmune encephalomyelitis
730 (EAE) as a model for multiple sclerosis (MS). *Br. J. Pharmacol.* **164**, 1079–1106 (2011).

731 47. N. M. O'Brown, S. G. Megason, C. Gu, Suppression of transcytosis regulates zebrafish blood-brain
732 barrier function. *eLife* **8**, e47326 (2019).

733 48. C. E. Shiau, K. R. Monk, W. Joo, W. S. Talbot, An Anti-inflammatory NOD-like Receptor Is
734 Required for Microglia Development. *Cell Rep.* **5**, 1342–1352 (2013).

735 49. L. Zhao, Z. Li, J. S. L. Vong, X. Chen, H.-M. Lai, L. Y. C. Yan, J. Huang, S. K. H. Sy, X. Tian, Y.
736 Huang, H. Y. E. Chan, H.-C. So, W.-L. Ng, Y. Tang, W.-J. Lin, V. C. T. Mok, H. Ko,
737 Pharmacologically reversible zonation-dependent endothelial cell transcriptomic changes with
738 neurodegenerative disease associations in the aged brain. *Nat. Commun.* **11**, 4413 (2020).

739 50. B. Rossi, S. Angiari, E. Zenaro, S. L. Budui, G. Constantin, Vascular inflammation in central nervous
740 system diseases: adhesion receptors controlling leukocyte-endothelial interactions. *J. Leukoc. Biol.*
741 **89**, 539–556 (2011).

742 51. W. A. Muller, Getting Leukocytes to the Site of Inflammation. *Vet. Pathol.* **50**, 7–22 (2013).

743 52. S. Nourshargh, R. Alon, Leukocyte Migration into Inflamed Tissues. *Immunity* **41**, 694–707 (2014).

744 53. A. Ben-Zvi, B. Lacoste, E. Kur, B. J. Andreone, Y. Mayshar, H. Yan, C. Gu, Mfsd2a is critical for
745 the formation and function of the blood–brain barrier. *Nature* **509**, 507–511 (2014).

746 54. R. Daneman, D. Agalliu, L. Zhou, F. Kuhnert, C. J. Kuo, B. A. Barres, Wnt/β-catenin signaling is
747 required for CNS, but not non-CNS, angiogenesis. *Proc. Natl. Acad. Sci.* **106**, 641–646 (2009).

748 55. J. M. Stenman, J. Rajagopal, T. J. Carroll, M. Ishibashi, J. McMahon, A. P. McMahon, Canonical
749 Wnt Signaling Regulates Organ-Specific Assembly and Differentiation of CNS Vasculature. *Science*
750 **322**, 1247–1250 (2008).

751 56. S. Liebner, M. Corada, T. Bangsow, J. Babbage, A. Taddei, C. J. Czupalla, M. Reis, A. Felici, H.
752 Wolburg, M. Fruttiger, M. M. Taketo, H. von Melchner, K. H. Plate, H. Gerhardt, E. Dejana, Wnt/β-
753 catenin signaling controls development of the blood–brain barrier. *J. Cell Biol.* **183**, 409–417 (2008).

754 57. H. Yousef, C. J. Czupalla, D. Lee, M. B. Chen, A. N. Burke, K. A. Zera, J. Zandstra, E. Berber, B.
755 Lehallier, V. Mathur, R. V. Nair, L. N. Bonanno, A. C. Yang, T. Peterson, H. Hadeiba, T. Merkel, J.
756 Körbelin, M. Schwaninger, M. S. Buckwalter, S. R. Quake, E. C. Butcher, T. Wyss-Coray, Aged
757 blood impairs hippocampal neural precursor activity and activates microglia via brain endothelial cell
758 VCAM1. *Nat. Med.* **25**, 988–1000 (2019).

759 58. H. Kim, K. Leng, J. Park, A. G. Sorets, S. Kim, A. Shostak, R. J. Embalabala, K. Mlouk, K. A.
760 Katdare, I. V. L. Rose, S. M. Sturgeon, E. H. Neal, Y. Ao, S. Wang, M. V. Sofroniew, J. M. Brunger,
761 D. G. McMahon, M. S. Schrag, M. Kampmann, E. S. Lippmann, Reactive astrocytes transduce
762 inflammation in a blood-brain barrier model through a TNF-STAT3 signaling axis and secretion of
763 alpha 1-antichymotrypsin. *Nat. Commun.* **13**, 6581 (2022).

764 59. S. Jin, C. F. Guerrero-Juarez, L. Zhang, I. Chang, R. Ramos, C.-H. Kuan, P. Myung, M. V. Plikus, Q.
765 Nie, Inference and analysis of cell-cell communication using CellChat. *Nat. Commun.* **12**, 1088
766 (2021).

767 60. H. D. Mason, D. B. McGavern, How the immune system shapes neurodegenerative diseases. *Trends*
768 *Neurosci.* **45**, 733–748 (2022).

769 61. T. R. Hammond, S. E. Marsh, B. Stevens, Immune Signaling in Neurodegeneration. *Immunity* **50**,
770 955–974 (2019).

771 62. M. P. Bevilacqua, Endothelial-Leukocyte Adhesion Molecules. *Annu. Rev. Immunol.* **11**, 767–804
772 (1993).

773 63. W. F. Hickey, B. L. Hsu, H. Kimura, T-lymphocyte entry into the central nervous system. *J. Neurosci.*
774 *Res.* **28**, 254–260 (1991).

775 64. K. Rössler, C. Neuchrist, K. Kitz, O. Scheiner, D. Kraft, H. Lassmann, Expression of leucocyte
776 adhesion molecules at the human blood-brain barrier (BBB). *J. Neurosci. Res.* **31**, 365–374 (1992).

777 65. G. Yilmaz, D. N. Granger, Cell adhesion molecules and ischemic stroke. *Neurol. Res.* **30**, 783–793
778 (2008).

779 66. T. K. Roberts, Leukocyte transmigration across the blood-brain barrier: perspectives on neuroAIDS.
780 *Front. Biosci.* **15**, 478 (2010).

781 67. B. W. Dulken, M. T. Buckley, P. Navarro Negredo, N. Saligrama, R. Cayrol, D. S. Leeman, B. M.
782 George, S. C. Boutet, K. Hebestreit, J. V. Pluvinage, T. Wyss-Coray, I. L. Weissman, H. Vogel, M.

M. Davis, A. Brunet, Single-cell analysis reveals T cell infiltration in old neurogenic niches. *Nature* **571**, 205–210 (2019).

68. M. B. Chen, A. C. Yang, H. Yousef, D. Lee, W. Chen, N. Schaum, B. Lehallier, S. R. Quake, T. Wyss-Coray, Brain Endothelial Cells Are Exquisite Sensors of Age-Related Circulatory Cues. *Cell Rep.* **30**, 4418-4432.e4 (2020).

69. A. C. Hedman, J. M. Smith, D. B. Sacks, The biology of IQGAP proteins: beyond the cytoskeleton. *EMBO Rep.* **16**, 427–446 (2015).

70. A. Sen, S. Youssef, K. Wendt, S. Anakk, Depletion of IQ motif-containing GTPase activating protein 2 (IQGAP2) reduces hepatic glycogen and impairs insulin signaling. *J. Biol. Chem.* **299**, 105322 (2023).

71. Yanyun Xie, Anil Kapoor, Hao Peng, Jean-Claude Cutz, Lijian Tao, Damu Tang, IQGAP2 Displays Tumor Suppression Functions. *J. Anal. Oncol.* **4** (2015).

72. L. Xu, Y. Shao, L. Ren, X. Liu, Y. Li, J. Xu, Y. Ye, IQGAP2 Inhibits Migration and Invasion of Gastric Cancer Cells via Elevating SHIP2 Phosphatase Activity. *Int. J. Mol. Sci.* **21**, 1968 (2020).

73. Y. Xie, L. Zheng, L. Tao, Downregulation of IQGAP2 Correlates with Prostate Cancer Recurrence and Metastasis. *Transl. Oncol.* **12**, 236–244 (2019).

74. F. Song, R. Kotolloshi, M. Gajda, M. Hölzer, M.-O. Grimm, D. Steinbach, Reduced IQGAP2 Promotes Bladder Cancer through Regulation of MAPK/ERK Pathway and Cytokines. *Int. J. Mol. Sci.* **23**, 13508 (2022).

75. Q. Dai, F. Song, X. Li, F. Huang, H. Zhao, Comprehensive analysis of the expression and prognosis for IQ motif-containing GTPase-activating proteins in hepatocellular carcinoma. *BMC Cancer* **22**, 1121 (2022).

76. Z. Deng, L. Wang, H. Hou, J. Zhou, X. Li, Epigenetic regulation of IQGAP2 promotes ovarian cancer progression via activating Wnt/β-catenin signaling. *Int. J. Oncol.* **48**, 153–160 (2016).

77. M. Uhlén, L. Fagerberg, B. M. Hallström, C. Lindskog, P. Oksvold, A. Mardinoglu, Å. Sivertsson, C. Kampf, E. Sjöstedt, A. Asplund, I. Olsson, K. Edlund, E. Lundberg, S. Navani, C. A.-K. Szigyarto, J. Odeberg, D. Djureinovic, J. O. Takanen, S. Hober, T. Alm, P.-H. Edqvist, H. Berling, H. Tegel, J. Mulder, J. Rockberg, P. Nilsson, J. M. Schwenk, M. Hamsten, K. von Feilitzen, M. Forsberg, L. Persson, F. Johansson, M. Zwahlen, G. von Heijne, J. Nielsen, F. Pontén, Tissue-based map of the human proteome. *Science* **347**, 1260419 (2015).

78. X. Chen, M. Firulyova, M. Manis, J. Herz, I. Smirnov, E. Aladyeva, C. Wang, X. Bao, M. B. Finn, H. Hu, I. Shchukina, M. W. Kim, C. M. Yuede, J. Kipnis, M. N. Artyomov, J. D. Ulrich, D. M. Holtzman, Microglia-mediated T cell infiltration drives neurodegeneration in tauopathy. *Nature* **615**, 668–677 (2023).

79. X. Zhang, R. Wang, H. Chen, C. Jin, Z. Jin, J. Lu, L. Xu, Y. Lu, J. Zhang, L. Shi, Aged microglia promote peripheral T cell infiltration by reprogramming the microenvironment of neurogenic niches. *Immun. Ageing* **19**, 34 (2022).

820 80. M. Jorfi, J. Park, C. K. Hall, C.-C. J. Lin, M. Chen, D. Von Maydell, J. M. Kruskop, B. Kang, Y.
821 Choi, D. Prokopenko, D. Irimia, D. Y. Kim, R. E. Tanzi, Infiltrating CD8+ T cells exacerbate
822 Alzheimer's disease pathology in a 3D human neuroimmune axis model. *Nat. Neurosci.* **26**, 1489–
823 1504 (2023).

824 81. Y.-K. Lee, H. Uchida, H. Smith, A. Ito, T. Sanchez, The isolation and molecular characterization of
825 cerebral microvessels. *Nat. Protoc.* **14**, 3059–3081 (2019).

826 82. M. Westerfield, *The Zebrafish Book: A Guide for the Laboratory Use of Zebrafish (Brachydanio*
827 *Rerio)* (1993).

828 83. N. C. Chi, R. M. Shaw, S. De Val, G. Kang, L. Y. Jan, B. L. Black, D. Y. R. Stainier, Foxn4 directly
829 regulates tbx2b expression and atrioventricular canal formation. *Genes Dev.* **22**, 734–739 (2008).

830 84. F. Ellett, L. Pase, J. W. Hayman, A. Andrianopoulos, G. J. Lieschke, mpeg1 promoter transgenes
831 direct macrophage-lineage expression in zebrafish. *Blood* **117**, e49-56 (2011).

832 85. W. Romero-Fernandez, C. Carvajal-Tapia, A. Prusky, K. A. Katdare, E. Wang, A. Shostak, L.
833 Ventura-Antunes, H. J. Harmsen, E. S. Lippmann, K. Fuxe, J. A. MacGurn, D. O. Borroto-Escuela,
834 M. S. Schrag, Detection, visualization and quantification of protein complexes in human Alzheimer's
835 disease brains using proximity ligation assay. *Sci. Rep.* **13**, 11948 (2023).

836 86. A. G. Nackenoff, T. J. Hohman, S. M. Neuner, C. S. Akers, N. C. Weitzel, A. Shostak, S. M. Ferguson,
837 B. Mobley, D. A. Bennett, J. A. Schneider, A. L. Jefferson, C. C. Kaczorowski, M. S. Schrag, PLD3
838 is a neuronal lysosomal phospholipase D associated with β-amyloid plaques and cognitive function
839 in Alzheimer's disease. *PLOS Genet.* **17**, e1009406 (2021).

840 87. E. Becht, L. McInnes, J. Healy, C.-A. Dutertre, I. W. H. Kwok, L. G. Ng, F. Ginhoux, E. W. Newell,
841 Dimensionality reduction for visualizing single-cell data using UMAP. *Nat. Biotechnol.* **37**, 38–44
842 (2019).

843 88. C. S. McGinnis, L. M. Murrow, Z. J. Gartner, DoubletFinder: Doublet Detection in Single-Cell RNA
844 Sequencing Data Using Artificial Nearest Neighbors. *Cell Syst.* **8**, 329-337.e4 (2019).

845 89. T. Stuart, A. Butler, P. Hoffman, C. Hafemeister, E. Papalexi, W. M. Mauck, Y. Hao, M. Stoeckius,
846 P. Smibert, R. Satija, Comprehensive Integration of Single-Cell Data. *Cell* **177**, 1888-1902.e21
847 (2019).

848 90. D. Aran, A. P. Looney, L. Liu, E. Wu, V. Fong, A. Hsu, S. Chak, R. P. Naikawadi, P. J. Wolters, A.
849 R. Abate, A. J. Butte, M. Bhattacharya, Reference-based analysis of lung single-cell sequencing
850 reveals a transitional profibrotic macrophage. *Nat. Immunol.* **20**, 163–172 (2019).

851 91. Y. Liao, J. Wang, E. J. Jaehnig, Z. Shi, B. Zhang, WebGestalt 2019: gene set analysis toolkit with
852 revamped UIs and APIs. *Nucleic Acids Res.* **47**, W199–W205 (2019).

853 92. K. Blighe, S. Rana, M. Lewis, EnhancedVolcano: publication-ready volcano plots with enhanced
854 colouring and labeling, (2018);
855 https://bioconductor.org/packages/release/bioc/vignettes/EnhancedVolcano/inst/doc/EnhancedVolca
856 no.html.

93. A. Lex, N. Gehlenborg, H. Strobelt, R. Vuillemot, H. Pfister, UpSet: Visualization of Intersecting Sets. *IEEE Trans. Vis. Comput. Graph.* **20**, 1983–1992 (2014).

94. G. Csardi, T. Nepusz, The igraph software package for complex network research. *InterJournal* **Complex Systems**, 1695 (2006).